Available online at www.sciencedirect.com
SCIENCE DIRECT®
Wave Motion 39 (2004) 61–75
WAVE MOTION
www.elsevier.com/locate/wavemoti

A model for the ultrasonic detection of surface-breaking cracks by the scanning laser source technique

Irene Arias*, Jan D. Achenbach

Center for Quality Engineering and Failure Prevention, Northwestern University, Evanston, IL 60208, USA

Received 22 February 2003; accepted 20 June 2003

Abstract

A model for the scanning laser source (SLS) technique is presented. The SLS is a novel laser-based inspection method for the ultrasonic detection of small surface-breaking cracks. The generated ultrasonic signal is monitored as a line-focused laser is scanned over the defect. Characteristic changes in the amplitude and the frequency content are observed. The modeling approach is based on the decomposition of the field generated by the laser in a cracked two-dimensional half-space, by virtue of linear superposition, into the incident and the scattered fields. The incident field is that generated by laser illumination of a defect-free half-space. A thermoelastic model has been used which takes account of the effect of thermal diffusion, as well as the finite width and duration of the laser source. The scattered field incorporates the interactions of the incident field with the surface-breaking crack. It has been analyzed numerically by a direct frequency domain boundary element method. A comparison with an experiment for a large defect shows that the model captures the observed phenomena. A simulation for a small crack illustrates the ability of the SLS technique to detect defects smaller than the wavelength of the generated Rayleigh wave.

Keywords: Laser ultrasonics; Thermoelastic regime; Line-source; Modeling; NDE; Surface-breaking crack; Crack detection; Scanning laser source technique

1. Introduction

Ultrasound has been widely applied in the field of non-destructive evaluation for the detection and characterization of anomalies of various kinds. Since the 1960s, pulsed lasers have emerged as an alternative to traditional techniques for the generation and detection of ultrasound. There are generally two mechanisms for such wave generation, depending on the amount of energy deposition by the laser pulse, namely ablation at very high power, and thermoelastic generation at moderate power operation. The latter does not damage the surface of the material, and is therefore suitable for applications in non-destructive evaluation (NDE).

The generation of ultrasound by laser irradiation provides a number of advantages over the conventional generation by piezoelectric transducers, namely high spatial resolution, non-contact generation and detection of ultrasonic waves, use of fiber optics, narrow-band and broad-band generation, absolute measurements, and ability to operate on curved and rough surfaces and at hard-to-access locations. On the receiving side, surface ultrasonic waves can

* Corresponding author. Present address: Graduate Aeronautical Laboratories, California Institute of Technology, 1200 East California Blvd., Pasadena CA 91125, USA. Tel.: +1-626-395-4757.
E-mail addresses: irene@aero.caltech.edu (I. Arias), achenbach@northwestern.edu (J.D. Achenbach).

0165-2125/$ – see front matter © 2003 Elsevier B.V. All rights reserved.
doi:10.1016/j.wavemoti.2003.06.001

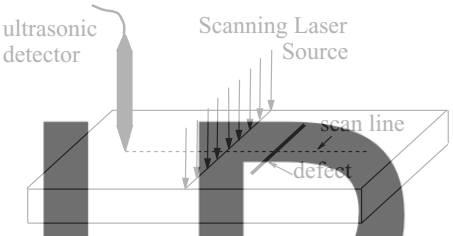

Fig. 1. Configuration for the SLS technique.

be detected using piezoelectric (PZT) or EMAT transducers, or optical interferometers in a completely laser-based system. Ultrasound generated by laser irradiation contains a large component of surface wave motion, and is therefore particularly useful for the detection of surface-breaking cracks.

The laser illumination of a pristine surface generates a well-defined wave package. Traditional techniques for the detection of surface-breaking cracks rely on monitoring the reflections (pulse-echo) or the changes in the amplitude of the transmission (pitch-catch) of this given incident signal caused by the presence of a defect. Nevertheless, for small defects relative to the wavelength of the generated Rayleigh wave, these reflections and changes in the transmission are often too weak to be detected with existing laser detectors. The recently proposed scanning laser source technique (SLS) provides an alternative inspection method which overcomes these size limitations [1].

The scanning laser source (SLS) technique employs a line-focused high-power laser source which is swept across the test specimen and passes over surface-breaking anomalies [2–4]. The generated ultrasonic waves are detected with an ultrasonic detector located either at a fixed distance from the laser source or at a fixed position on the test specimen. Fig. 1 sketches the inspection technique. The distinguishing feature of this method is that it monitors the changes in the laser generated signal as the illuminated region is swept over a defect, rather than the interactions of a well-established incident signal with the defect. The presence of a flaw modifies the generation conditions and produces reflections, leading to clear differences in the shape of the signal, its amplitude, and its frequency content, as compared to the signal generated on a defect-free surface. Thus, a distinct signature of the defect can be observed in the peak-to-peak amplitude and maximum frequency of the generated signal as the laser passes over the defect, as illustrated in the experimental observations and numerical simulations presented later in this paper. There is experimental evidence that this signature is noticeable even for cracks much smaller than the detection threshold for conventional methods and for arbitrary orientation of the crack with respect to the direction of scanning [2].

In this paper, a model for the SLS technique is presented and compared against experiments. The objective is to identify the relevant physical mechanisms responsible for the observed behavior, and possibly optimize the inspection technique. A scanning laser line-source whose axis is parallel to a relatively long surface-breaking crack in a structure is considered. This situation is modeled as a two-dimensional, plane strain thermoelastic problem and the test specimen is approximated by a homogeneous, isotropic, linearly elastic half-space. The surface-breaking crack is assumed to be mathematically sharp and perpendicular to the surface of the half-space. In [5], the SLS technique in the above situation has been analyzed numerically by modeling the wave propagation phenomena with a two-dimensional mass spring lattice model, and the line-focused laser source with a simplified shear dipole model which neglects thermal diffusion. Here, by virtue of linear superposition, the field generated by the line-focused laser source in the presence of the defect is decomposed into the incident and the scattered fields (see Fig. 2).

The incident field is that generated by line-focused laser illumination of the half-space in the absence of the defect, and is treated as a thermoelastic problem. The scattered field is defined as the field generated in the cracked half-space by tractions acting on the crack faces that cancel out those produced by the laser line-source on the same plane, so that the condition of traction free crack faces is met after the superposition of the incident and the scattered fields. Each problem is solved separately.

The problem of the incident field is that of thermoelastic laser generation of ultrasound under plane strain conditions. Since the 1960s researchers have been studying the generation of ultrasound by lasers [6]. Many models

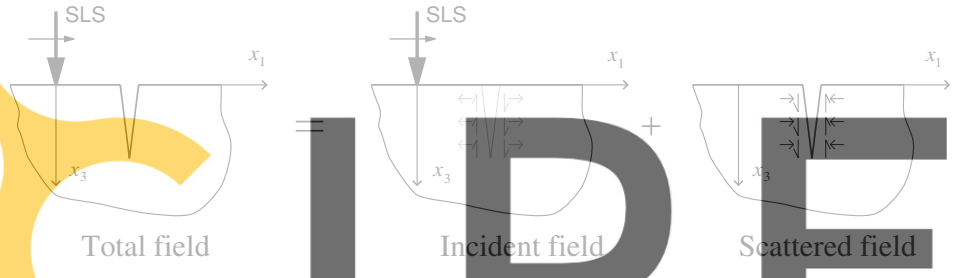

Fig. 2. Decomposition of the total field into incident and scattered fields.

have been developed, most of them defining an elastic source equivalent to the laser source, and thereby neglecting its thermoelastic nature. As pointed out by earlier authors [7], intuitively the actions of a local generation of a temperature field and the application of an elastic shear dipole acting on the surface should be expected to produce equivalent fields. This approximation assumes that all the energy is deposited at the surface and does not diffuse. Thus, it neglects the two basic physical mechanisms through which thermal energy penetrates into the bulk of material giving rise to subsurface thermal sources, namely optical absorption of the laser energy into the bulk material and thermal diffusion from the heat source. The subsurface thermal sources have a localized effect which is significant near the laser source and becomes negligible far away from it. Therefore, while the purely elastic shear dipole model provides a good approximation of the far-field, it is unable to accurately predict the near-field. This fact becomes particularly noticeable in its inability to predict a basic feature of the near-field, the so-called precursor. The precursor is a small, but relatively sharp initial spike observed experimentally at the longitudinal wave arrival, which has been related to the presence of subsurface sources [8]. In the context of the SLS technique, the laser generated field has to be determined accurately as the source approaches the position of the crack, since the tractions generated on the plane that represents the position of the crack are the input for the scattering problem. Therefore, it is clear that, for our purposes, the effects of subsurface deposition of energy need to be included in the formulation of the problem of the incident field.

In [9], a two-dimensional model for the line-focused laser generation of ultrasound was developed based on a unified treatment of the thermoelastic problem in plane strain. This model takes account of the finite width of the source, the temporal shape of the pulse and the subsurface sources arising from thermal diffusion and optical penetration. The thermoelastic problem in a homogeneous, isotropic, linearly elastic half-space is solved analytically in the Fourier–Laplace transform domain. The doubly transformed solution is inverted numerically to produce theoretical waveforms. The shear dipole model follows from appropriate limits. This thermoelastic model is used here to obtain an accurate description of the incident field in a metallic half-space. In metals, the subsurface sources arise mainly from thermal diffusion, since the optical absorption depth is very small compared to the thermal diffusion length. Thus, the limit case of strong optical absorption is considered. The corresponding formulation is detailed in Section 2 and some basic results relevant to the modeling of the SLS technique are presented.

The scattered field is defined as that generated on the cracked half-space by suitable tractions acting on the faces of the crack. These tractions are equal an opposite to those generated by the incident field in the uncracked half-space when evaluated on the plane of the crack. By defining the scattered field in this manner, it is assumed that the crack does not affect the diffusion of heat in the specimen. This assumption allows for the coupled thermoelastic scattering problem to be reduced to an isothermal elastic problem of two-dimensional wave diffraction by a surface-breaking crack in a half-space. This simplification is considered to be realistic for small fatigue cracks and has proven to be sufficiently accurate. The scattering problem is solved numerically by a direct frequency domain boundary element method (BEM). The details are presented in Section 3.

The two problems are solved separately to obtain vertical surface displacements waveforms for the incident and the scattered field at the receiver location. The superposition of these waveforms yields the theoretical SLS time signal for a certain position of the source. Then different SLS positions are considered and the peak-to-peak

amplitude of each corresponding signal is plotted versus the SLS position to construct the theoretical amplitude signatures. Similarly, by considering the frequency content of each signal and plotting the maximum frequency versus SLS position, the frequency signature of the crack in the SLS technique is generated.

2. The incident field

The thermoelastic problem is formulated in the context of the generalized theory of thermoelasticity which assumes a hyperbolic description of heat conduction. The governing equations of the thermal and the elastic problems are in principle doubly coupled. However, in the thermoelastic regime, the heat produced by mechanical deformation can be neglected. With this so-called thermal stress approximation, the equations are coupled only one-way through the thermal stress term. The governing equations for an isotropic solid are

$$\nabla^2 T - \frac{1}{\kappa}\dot{T} - \frac{1}{c^2}\ddot{T} = -\frac{q}{k}, \tag{1}$$

$$\mu\nabla^2\mathbf{u} + (\lambda+\mu)\nabla(\nabla\cdot\mathbf{u}) = \rho\ddot{\mathbf{u}} + \beta\nabla T \tag{2}$$

where T is the absolute temperature, $\mathbf{u}$ the displacement vector field, κ the thermal diffusivity, c the heat propagation speed which is taken to be equal to the longitudinal wave speed (see [9] for details), k the thermal conductivity, β the thermoacoustic coupling constant: $\beta = (3\lambda + 2\mu)\alpha_T$, α_T is the coefficient of linear thermal expansion and q the heat source due to laser line-source illumination. A suitable expression for the surface heat deposition q in the solid along an infinitely long line is

$$q = E(1 - R_i)\, f(x_1) g(t), \tag{3}$$

with

$$f(x_1) = \frac{1}{\sqrt{2\pi}}\frac{2}{R_G}\mathrm{e}^{-2x_1^2/R_G^2}, \tag{4}$$

and

$$g(t) = \frac{8t^3}{\upsilon^4}\mathrm{e}^{-2t^2/\upsilon^2}, \tag{5}$$

where E is the energy of the laser pulse per unit length, R_i the surface reflectivity, R_G the Gaussian beam radius, υ the laser pulse risetime (full width at half maximum). The coordinate axis x_1 is directed along the surface perpendicularly to the line-source, and x_3 normal to the surface pointing inwards.

Eq. (3) represents a strip of illumination since it is defined by a Gaussian in x_1. The Gaussian does not vanish completely with distance, but its value becomes negligible outside a strip. The source is spread out in time according to the function proposed by Schleichert et al. [10]. For both the temporal and the spatial profile, the functional dependence has been constructed so that in the limit $\upsilon \to 0$ and $R_G \to 0$, an equivalent concentrated line-source is obtained.

The system of governing equations, which we consider in the plane strain approximation for the case of an infinitely long line-source, must be supplemented by initial and boundary conditions. The initial conditions are that the half-space is initially at rest. The boundary conditions include thermal and mechanical conditions. If the boundary is defined by $x_3 = 0$, then the considered thermal boundary condition is

$$\frac{\partial T}{\partial x_3} = 0, \quad \text{at } x_3 = 0. \tag{6}$$

This condition implies that heat does not flow into or out of the half-space via the boundary. The heat that is generated by the laser is deposited inside the half-space just under the surface. The mechanical boundary condition is that the tractions are zero on the surface ($x_3 = 0$), i.e.

$$\sigma_{31} = \mu(u_{3,1} + u_{1,3}) = 0, \quad \text{at } x_3 = 0, \tag{7}$$

$$\sigma_{33} = \lambda(u_{1,1} + u_{3,3}) + 2\mu u_{3,3} - \beta\Delta T = 0, \quad \text{at } x_3 = 0. \tag{8}$$

Eqs. (1) and (2) with the above boundary and initial conditions are solved using standard Fourier–Laplace transform techniques for two-dimensional, time-dependent systems. The problem is first reformulated in terms of the usual displacement potentials: the dilatational potential ϕ and the rotational potential $\psi = \nabla \times (0, 0, \psi)$, where ψ is set to satisfy the homogenous scalar wave equation. The exponential Fourier transform in the spatial coordinate x_1 and the one-sided Laplace transform in time are then applied to the governing equations, and the boundary and initial conditions. A closed form solution is obtained for the transformed potentials. The transformed displacements and stresses can be derived from the solution for the transformed potentials. The expressions in the limit case of strong optical absorption are

$$\tilde{\bar{u}}_1 = \mathrm{i}p\frac{\Gamma\kappa}{sR}\left\{M\,\mathrm{e}^{-\zeta x_3} + 2\eta(\eta^2+p^2)\left(1-\frac{\zeta}{\xi}\right)\mathrm{e}^{-\eta x_3} - \frac{R}{\xi}\mathrm{e}^{-\xi x_3}\right\}, \tag{9}$$

$$\tilde{\bar{u}}_3 = \frac{\Gamma\kappa}{sR}\left\{M\zeta\,\mathrm{e}^{-\zeta x_3} + 2p^2(\eta^2+p^2)\left(1-\frac{\zeta}{\xi}\right)\mathrm{e}^{-\eta x_3} - R\,\mathrm{e}^{-\xi x_3}\right\}, \tag{10}$$

$$\tilde{\bar{\sigma}}_{11} = \mu\frac{\Gamma\kappa}{sR}\left\{M(2\zeta^2 - b^2s^2)\,\mathrm{e}^{-\zeta x_3} + 4p^2\eta(\eta^2+p^2)\left(1-\frac{\zeta}{\xi}\right)\mathrm{e}^{-\eta x_3} + \frac{R}{\xi}(b^2s^2 - 2\xi^2)\,\mathrm{e}^{-\xi x_3}\right\}, \tag{11}$$

$$\tilde{\bar{\sigma}}_{33} = \mu\frac{\Gamma\kappa}{sR}(\eta^2+p^2)\left\{-M\,\mathrm{e}^{-\zeta x_3} - 4\eta p^2\left(1-\frac{\zeta}{\xi}\right)\mathrm{e}^{-\eta x_3} + \frac{R}{\xi}\mathrm{e}^{-\xi x_3}\right\}, \tag{12}$$

$$\tilde{\bar{\sigma}}_{13} = 2\mu\mathrm{i}p\frac{\Gamma\kappa}{sR}\left\{M\zeta\,\mathrm{e}^{-\zeta x_3} + (\eta^2+p^2)\left(1-\frac{\zeta}{\xi}\right)\mathrm{e}^{-\eta x_3} - R\,\mathrm{e}^{-\xi x_3}\right\}, \tag{13}$$

with $\zeta^2 = p^2 + a^2s^2$, $\eta^2 = p^2 + b^2s^2$, $\xi^2 = \zeta^2 + s/\kappa$, $R = (\eta^2+p^2)^2 - 4\zeta\eta p^2$, and $M = (\eta^2+p^2)^2/\xi - 4\eta p^2$. Also, $\Gamma = \beta Q_0 Q_p(p) Q_s(s)/(\lambda + 2\mu)$ and

$$Q_0 = \frac{E}{k}(1 - R_i), \tag{14}$$

$$Q_p(p) = \frac{1}{\sqrt{2\pi}}\mathrm{e}^{-p^2R_G^2/8}, \tag{15}$$

$$Q_s(s) = \mathcal{L}\left\{\frac{8t^3}{\upsilon^4}\mathrm{e}^{-2t^2/\upsilon^2}\right\}, \tag{16}$$

where $\mathcal{L}$ indicates Laplace transform, (t, s) is the Laplace pair and (x, p) the Fourier pair, λ and μ are the Lamé constants, a and b are the slownesses of the longitudinal and the transverse waves, respectively. The Laplace transformed and the Fourier transformed fields are denoted with a bar and a tilde, respectively.

The solutions for the displacements and tractions in the domain of Fourier–Laplace transformed variables provide insight into the physics of the problem. Eqs. (9)–(13) indicate three modes of energy transport, namely longitudinal waves (associated with the terms proportional to $\mathrm{e}^{-\zeta x_3}$), transverse waves (associated with the terms proportional to $\mathrm{e}^{-\eta x_3}$) and thermal diffusion (associated with the terms proportional to $\mathrm{e}^{-\xi x_3}$). These three mechanisms can be observed in the illustrative waveforms presented later in this section.

The solution in the transformed domain is then inverted numerically. The integral of the inverse Fourier transform is evaluated by using a Romberg integration routine with polynomial extrapolation [11]. The general method used for the numerical inversion of the Laplace transform is based on a technique developed in [12].

In order to model the SLS technique, the tractions on vertical planes located at different positions with respect to the laser line-source (input for scattering problem) need to be computed, as well as vertical surface displacements (incident field for superposition). Here, the values for the material properties correspond to aluminum alloy 2024-T6

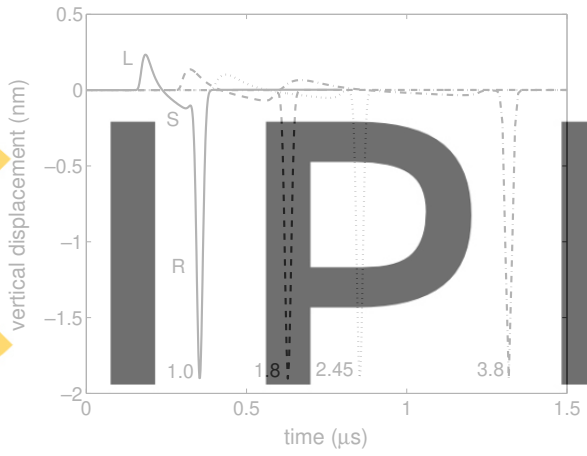

Fig. 2. Normal displacement on the surface. The numbers next to the wavefronts indicate the distance in mm from the axis of the laser line-source. The labels L, S and R denote longitudinal, shear and Rayleigh surface waves, respectively. A negative value represents an inward normal displacement.

and are: $c_L = 6.321\,\text{mm}/\mu\text{s}$, $c_T = 3.11\,\text{mm}/\mu\text{s}$, $\alpha_T = 2.2 \times 10^{-5}1/\text{K}$, $\kappa = 6.584 \times 10^{-5}\,\text{mm}^2/\mu\text{s}$, $k = 160\,\text{W}/\text{mK}$, $R_i = 91\%$. The parameters of the laser are: $E = 1\,\text{mJ}$ per unite length of the line-source, $R_G = 0.14\,\text{mm}$ and $\upsilon = 10\,\text{ns}$.

Fig. 3 displays the theoretical waveforms of surface normal displacement at four different distances from the axis of the laser line-source, where a negative displacement is in the positive x_3 direction, i.e. inwards. All the waveforms correspond to distances far from the irradiated region, so that the thermal effects are negligible. Thus, the predictions of the thermoelastic model show excellent agreement with those of the shear dipole model, as expected [9]. In the far-field, the waveforms are dominated by the Rayleigh surface wave which travels along the surface without geometrical attenuation. The Rayleigh pulse is a monopolar inward displacement, whose temporal profile reproduces that of the laser beam, in contrast with the bipolar Rayleigh pulse produced by a point-source. The attenuating longitudinal and shear waves can also be identified in the waveforms.

Fig. 4 shows the σ_{11} stress component on the surface at several distances from the axis of the laser line-source. The theoretical waveforms exhibit quite different behavior for small and large distances from the laser source. The stress field inside the heated region, i.e. $x_1 < 0.2\,\text{mm}$ in Fig. 4, is dominated by the thermal stresses generated by the laser induced temperature field, which diffuse into the material at a slower time scale as compared to the propagation of elastic waves. Well inside the irradiated region, i.e. $x_1 \leq 0.04\,\text{mm}$, a high compressive σ_{11} field is generated since the rapid expansion of the heated region is laterally constrained by the unheated surrounding material. Far away from the source the thermal effects are negligible and the propagation of elastic waves can be clearly identified. The Rayleigh surface wave induces a compressive σ_{11} pulse preceded and followed by smaller tensile pulses.

Fig. 5 shows theoretical waveforms at various depths of normal σ_{11} and shear σ_{31} tractions on two vertical planes: one close to the axis of the laser line-source (two left-most plots) and the other far from it (two right-most plots). In these figures, a negative normal stress indicates compression and a positive shear stress on the top face of an element points in the negative x_1 direction. Again, the shape of the waveforms is qualitatively quite different for small and large distances from the laser source. The thermal stresses are apparent in the near-field for small depths. The propagation of the different wavefronts at different speeds is also apparent.

It is clear that, since the generated fields differ near and far from the laser source, the corresponding scattered fields produced by the interaction of these fields with the crack will also be very sensitive to the distance to the laser source. The analysis of the incident field provides clues to interpret the experimental observations. For instance,

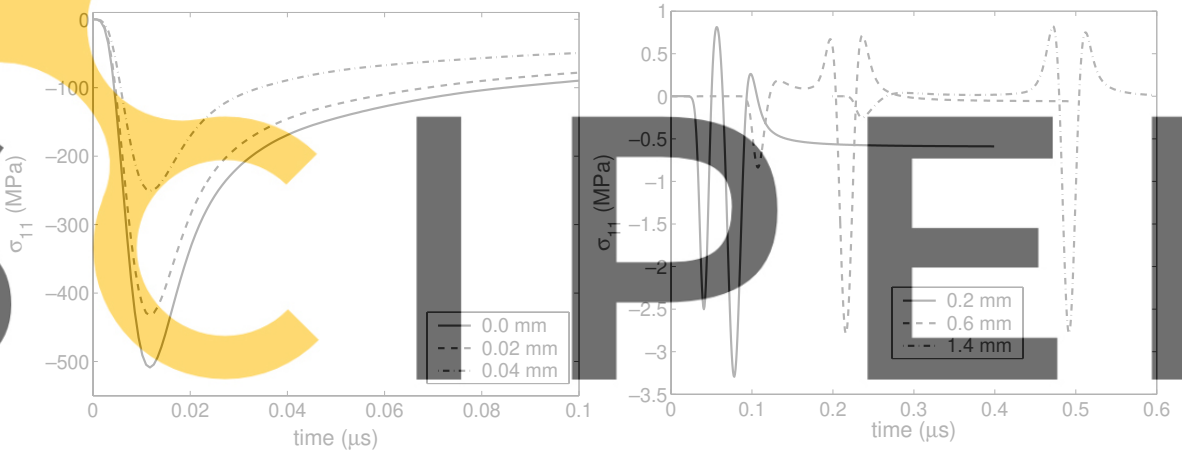

Fig. 4. Stress component σ_{11} on the surface. The legend indicates the distance to the epicentral axis. A negative value of σ_{11} indicates compression.

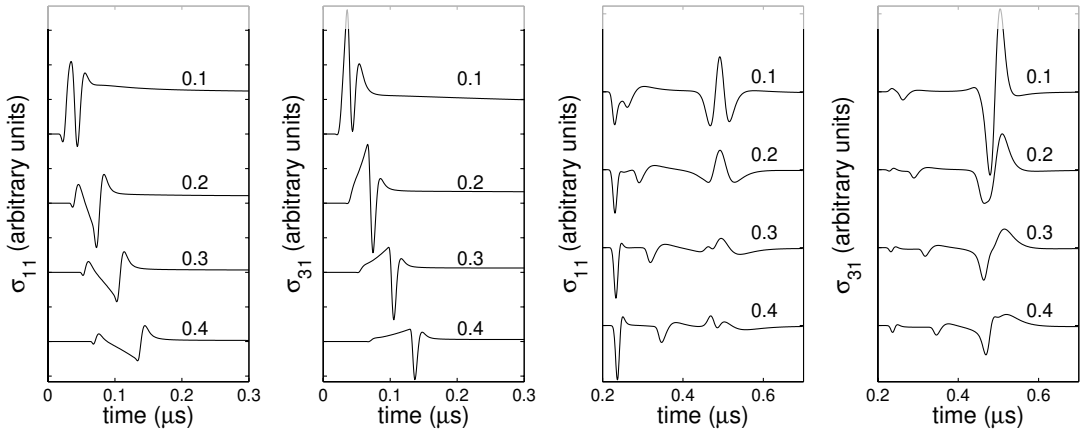

Fig. 5. Tractions on the vertical plane at 0.05 mm (left) and 1.4 mm (right) distance from the axis of the laser line-source at various depths. The numbers next to the waveforms indicate the depth in mm. A negative normal traction indicates compression and a positive shear traction on the top face of an element points in the negative x_1 direction.

analogously to the SLS crack signature in the maximum frequency evolution, the frequency content of the generated signal is shifted to higher frequencies as the distance to the laser source decreases and then drops for very small distances.

3. The scattered field

The interactions of a surface-breaking crack with the field generated by the laser in a half-space are analyzed next. By decomposing the scattered field into symmetric and anti-symmetric fields with respect to the plane of the crack, two initial boundary value problems for the quarter-space are obtained (see Fig. 6). The symmetric problem is defined by normal tractions acting on the plane of the crack which are equal and opposite to the ones generated by the incident field, whereas the anti-symmetric problem is defined by the corresponding shear tractions. Therefore,

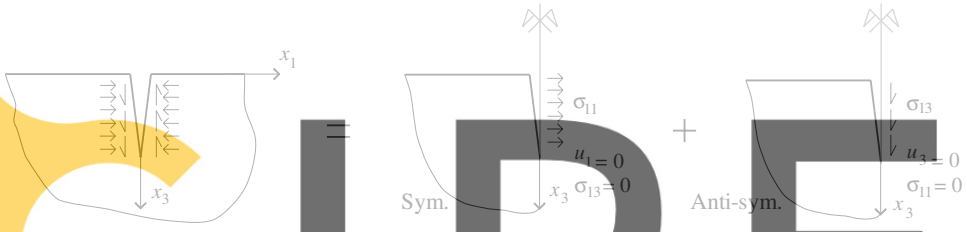

Fig. 6. Decomposition into the symmetric and the anti-symmetric problems in a quarter-space.

the boundary conditions at $x_1 = 0$ for each problem are

$$\sigma_{13}^{sc} = 0, \quad 0 \le x_3 < \infty, \qquad \sigma_{11}^{sc} = -\sigma_{11}^{in}, \quad 0 \le x_3 < a, \qquad u_1^{sc} = 0, \quad a \le x_3 < \infty \tag{17}$$

for the symmetric problem and

$$\sigma_{13}^{sc} = -\sigma_{13}^{in}, \quad 0 \le x_3 < a, \qquad \sigma_{11}^{sc} = 0, \quad 0 \le x_3 < \infty, \qquad u_3^{sc} = 0, \quad a \le x_3 < \infty \tag{18}$$

for the anti-symmetric problem, where the superscripts "sc" and "in" stand for the scattered, and the incident fields, respectively, and a is the length of the crack. For both the symmetric and the anti-symmetric problem, the surface of the quarter-space is free of tractions. In addition, it is required that the scattered field represents outgoing waves. The governing equation for a homogeneous, isotropic, linearly elastic solid is Eq. (2), which in the isothermal case reduces to

$$\mu\nabla^2\mathbf{u}^{sc}(\mathbf{x},t) + (\lambda+\mu)\nabla(\nabla\cdot\mathbf{u}^{sc})(\mathbf{x},t) = \rho\ddot{\mathbf{u}}^{sc}(\mathbf{x},t), \tag{19}$$

where $\mathbf{x} \in (-\infty, 0] \times [0, \infty)$ is the position vector and $t > 0$ represents time.

Each of these problems is solved numerically with a two-dimensional direct frequency domain quadratic boundary element method [13]. The symmetric and anti-symmetric problems are formulated in the frequency domain by the application of the Fourier transform to the equation and the boundary conditions, assuming a quiescent past. The resulting transformed equation of motion is

$$\mu\nabla^2\bar{\mathbf{u}}^{sc}(\mathbf{x},\omega) + (\lambda+\mu)\nabla(\nabla\cdot\bar{\mathbf{u}}^{sc})(\mathbf{x},\omega) + \rho\omega^2\bar{\mathbf{u}}^{sc}(\mathbf{x},\omega) = 0, \tag{20}$$

where ω stands for the angular frequency and the transformed displacement field is denoted with a bar. The corresponding boundary integral equations for a point $\boldsymbol{\xi}$ located on the boundary of the domain, Γ, are derived in the usual manner [14] as

$$c_{\alpha\beta}(\boldsymbol{\xi})\bar{u}_\beta^{sc}(\boldsymbol{\xi},\omega) = \int_\Gamma [\bar{u}_{\alpha\beta}^*(\boldsymbol{\xi},\mathbf{x},\omega)\bar{t}_\beta^{sc}(\mathbf{x},\omega) - \bar{t}_{\alpha\beta}^*(\boldsymbol{\xi},\mathbf{x},\omega)\bar{u}_\beta^{sc}(\mathbf{x},\omega)]\,\mathrm{d}\Gamma(\mathbf{x}), \quad \alpha,\beta = 1,2, \tag{21}$$

where $\bar{u}_{\alpha\beta}^*$ and $\bar{t}_{\alpha\beta}^*$ are the full-space frequency domain elastodynamic fundamental solution displacement and traction tensors respectively. Note that $\bar{u}_{\alpha\beta}^*(\boldsymbol{\xi},\mathbf{x},\omega)$ and $\bar{t}_{\alpha\beta}^*(\boldsymbol{\xi},\mathbf{x},\omega)$ represent the "β" component of the displacement and the traction on the boundary, respectively, at the point $\mathbf{x}$ due to a unit time-harmonic load of angular frequency ω applied at the point $\boldsymbol{\xi}$ in the direction "α". Also, $\bar{u}_\beta^{sc}$, $\bar{t}_\beta^{sc}$ are frequency domain displacements and tractions on the boundary, and $c_{\alpha\beta}$ is called the jump coefficient given by

$$c_{\alpha\beta}(\boldsymbol{\xi}) = \begin{cases} \frac{1}{2}\delta_{\alpha\beta}, & \text{if } \Gamma \text{ is smooth at } \boldsymbol{\xi}, \\ c_{\alpha\beta}, & \text{if } \Gamma \text{ has a corner at } \boldsymbol{\xi}, \end{cases} \tag{22}$$

where $\delta_{\alpha\beta}$ represents the Kronecker delta. The jump coefficient for corner points can be derived by an indirect approach as described in [14]. The integrals in Eq. (21) are interpreted in the sense of the Cauchy Principal Value.

The boundary integral equations are solved numerically for the symmetric and anti-symmetric transformed displacements and tractions on the boundary. The boundary of the domain is discretized using quadratic boundary elements and a quadratic interpolation of the transformed displacements and traction fields is introduced. A singular traction quarter-point boundary element has been used to reproduce the singular behavior of the stresses at the crack tip [15]. After solving the transformed problems, the transient solution is obtained by numerical inversion of the Fourier transform with a fast Fourier transform (FFT) algorithm.

Note that the above presented approach entails the solution of two initial boundary value problems on the quarter-space, instead of just one on the half-space. However, it avoids the well-known degeneracy of the conventional BEM for the flat cracks, which is essentially associated with the ill-posed nature of problems with two coplanar faces [16].

It has been shown that the sharpness of the laser line-source generated signal increases as the line becomes narrower or the laser pulse shorter [9]. For instance, in the limit of the shear dipole, the generated Rayleigh surface wave is a monopolar pulse propagating along the surface of the half-space which reproduces the shape of the laser pulse. The high-frequency content of the incident field for narrow lines and short pulses imposes stringent conditions on the number of frequencies to be computed for an accurate sampling in a given time window. The requirement of describing a wavelength with about 10 nodes results in a quite small element size. On the other hand, the experiments the receiver is located at sufficient distance from the crack to allow for the scanning of the specimen surface, and thus the region of interest, where accurate solutions are needed, can be relatively large, leading to a high number of elements. These facts lead to large computational meshes and, thus, high memory requirements and computational times. In efforts to reduce the computational time, the natural parallelism of the frequency domain approach has been exploited in the computer implementation.

The infinite surface of the quarter-space has to be truncated for numerical calculation purposes. The simple truncation introduces spurious reflections from the ends of the computational boundary that distort the numerical solution in the region close to the truncation point. Note that in a two-dimensional geometry, undamped Rayleigh waves do not exhibit geometrical attenuation, and will always produce reflections in a simply truncated mesh. This issue is typically addressed by extending the computational mesh far beyond the region of interest and adding a small amount of damping. In [17], a correction for the truncation of the infinite boundary has been formulated which allows the undamped Rayleigh waves to escape the computational domain without producing spurious reflections from its end nodes. This method exploits the knowledge of the asymptotic behavior of the solution—here Rayleigh surface waves are assumed to dominate the far-field solution—to adequately correct the BEM displacement system matrix for the truncated problem to account for the contribution of the omitted part of the boundary. The reciprocity theorem of elastodynamics allows for a convenient computation of this contribution involving the same element integrals that form the original BEM system. The proposed method is easy to implement and, in the case of a quarter-space, it comes at essentially no additional cost as compared to the simple truncation of the boundary. The accuracy of the solution provided by the proposed model depends on the accuracy of the assumption that Rayleigh waves strongly dominate at the end points of the computational domain. However, once the computational domain is extended far enough from the source region for this assumption to hold, the corrected solution, unlike the simply truncated solution, is accurate everywhere in the computational domain and for all computed times. In situations where the region of interest extends far beyond the source region where waves are generated, the proposed method reduces the extent of the computational boundary.

4. Representative examples

4.1. Comparison with experiment for a large notch

Sohn and Krishnaswamy [18] have carried out experiments on an aluminum specimen in the presence of a notch of 2.5 mm in depth and 0.3 mm in width. A Q-switched line-focused laser was used at 10 mJ energy deposition. The

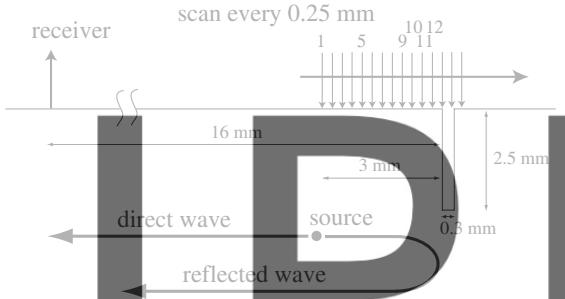

Fig. 7. Experimental setup for the SLS inspection of a notched specimen.

width of the illumination strip was estimated to be around 200 μm width by burn marks on photosensitive paper. The duration of the pulse was 70 ns. The laser source scanned the specimen from a distance of 3.0 mm from the left face of the notch to a distance of 0.5 mm past the left face of the notch. A laser detector was used to record surface normal displacements at a distance of 16 mm from the left face of the crack in each scanning step (see Fig. 7). Both the signals recorded at the receiver and the resulting peak-to-peak amplitude evolution with the position of the laser source were provided.

A numerical example inspired in this experiment is presented next. The notch has been replaced by a surface-breaking crack of the same depth in the plane of the left face of the notch. It has been verified, that this approximation does not have a significant effect on the response of the system at the receiver for a notch of this depth relative to the wavelengths of the generated Rayleigh wave. The material properties used in the simulation are: $c_L = 5.9\,\mathrm{mm/\mu s}$, $c_T = 3.1\,\mathrm{mm/\mu s}$, $\alpha_T = 2.2 \times 10^{-5}\,\mathrm{1/K}$, $\kappa = 1.0 \times 10^{-4}\,\mathrm{mm^2/\mu s}$, $k = 160\,\mathrm{W/mK}$, $R_i = 91\%$. There are uncertainties concerning the exact spatial and temporal distribution of the energy deposition. Thus, the parameters of the laser source model have been selected to approximately reproduce the direct signal from the laser source.

Figs. 8 and 9 show the experimental (left column), and the numerically predicted (right column) signals at the receiver when the laser is located at six different positions relative to the left face of the notch. The receiver is far enough so that most of the recorded waveforms correspond to Rayleigh waves. In the first plots, the monopolar direct signal and the reflection can be clearly distinguished. As the laser approaches the notch, these signals start to interfere with each other. An apparent increase in peak-to-peak amplitude and a sharp outward surface displacement can be observed when the laser is close to the crack. Experiment and simulation show good qualitative agreement. Better quantitative agreement would follow from further adjustment of the parameters of the model.

Fig. 10 shows the experimental and numerical evolution of the peak-to-peak amplitude. The characteristic signature of the discontinuity is well predicted by the model. Due to the large depth of the crack, a very small signal is predicted when the laser impinges of the right side of the notch. This signal cannot be distinguished from experimental records.

4.2. SLS simulation for a small surface-breaking crack

The illustrative theoretical analysis of a small surface-breaking crack of 0.4 mm depth is reported in this Section. The material and laser parameters are those of the example in Section 2, and the receiver is located at a distance of 2.4 mm from the plane of the crack. Fig. 12 shows the simulated time signal at the receiver corresponding to the three representative positions of the laser relative to the crack: far ahead (I), very close to (II) and far behind (III) the crack (see Fig. 11). Again, the qualitative features observed in experiments are reproduced by the model.

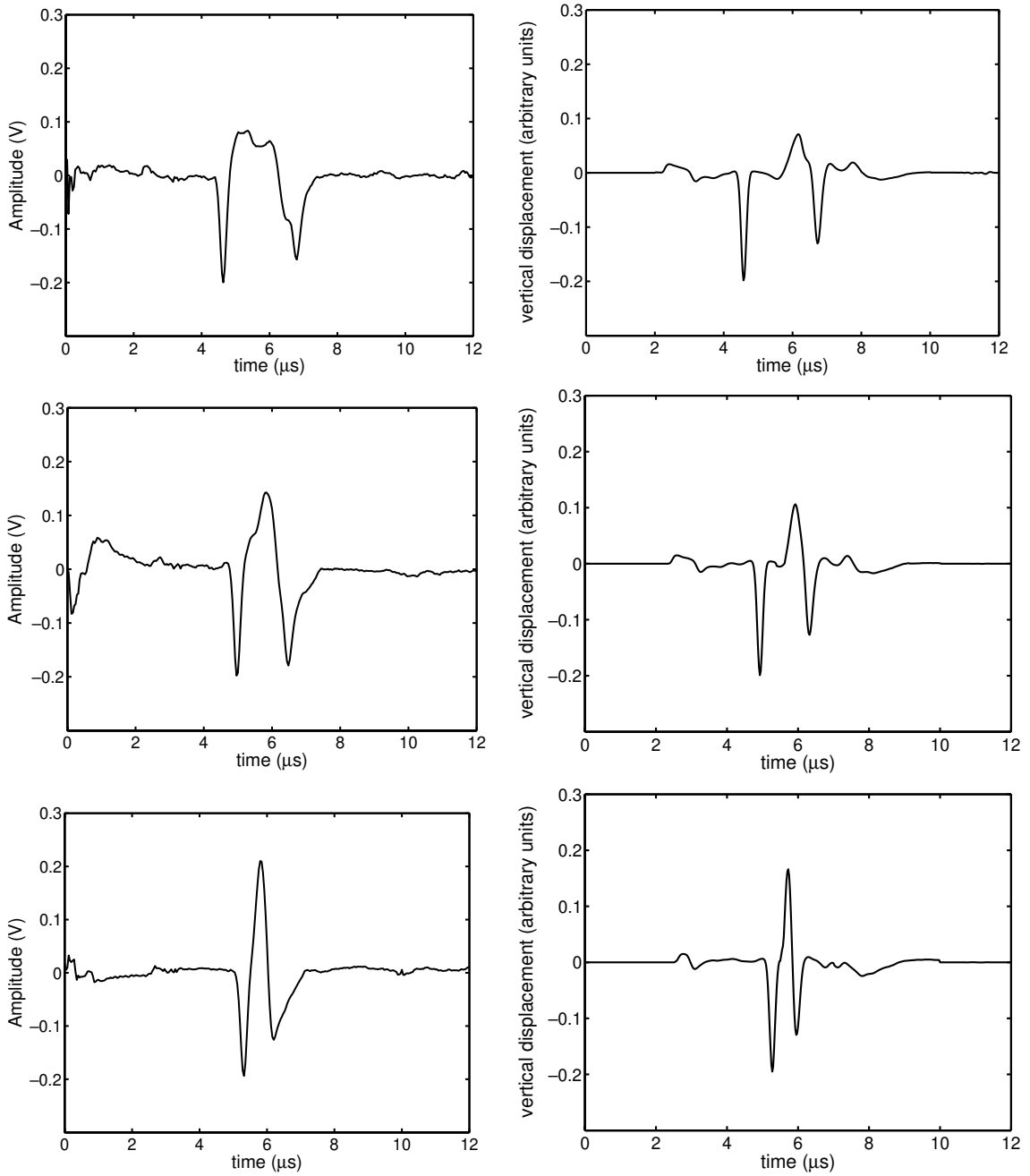

Fig. 8. Experimental (left column) and simulated (right column) signals at the receiver when the laser is located at distances of 3, 2 and 1 mm from the left face of the notch.

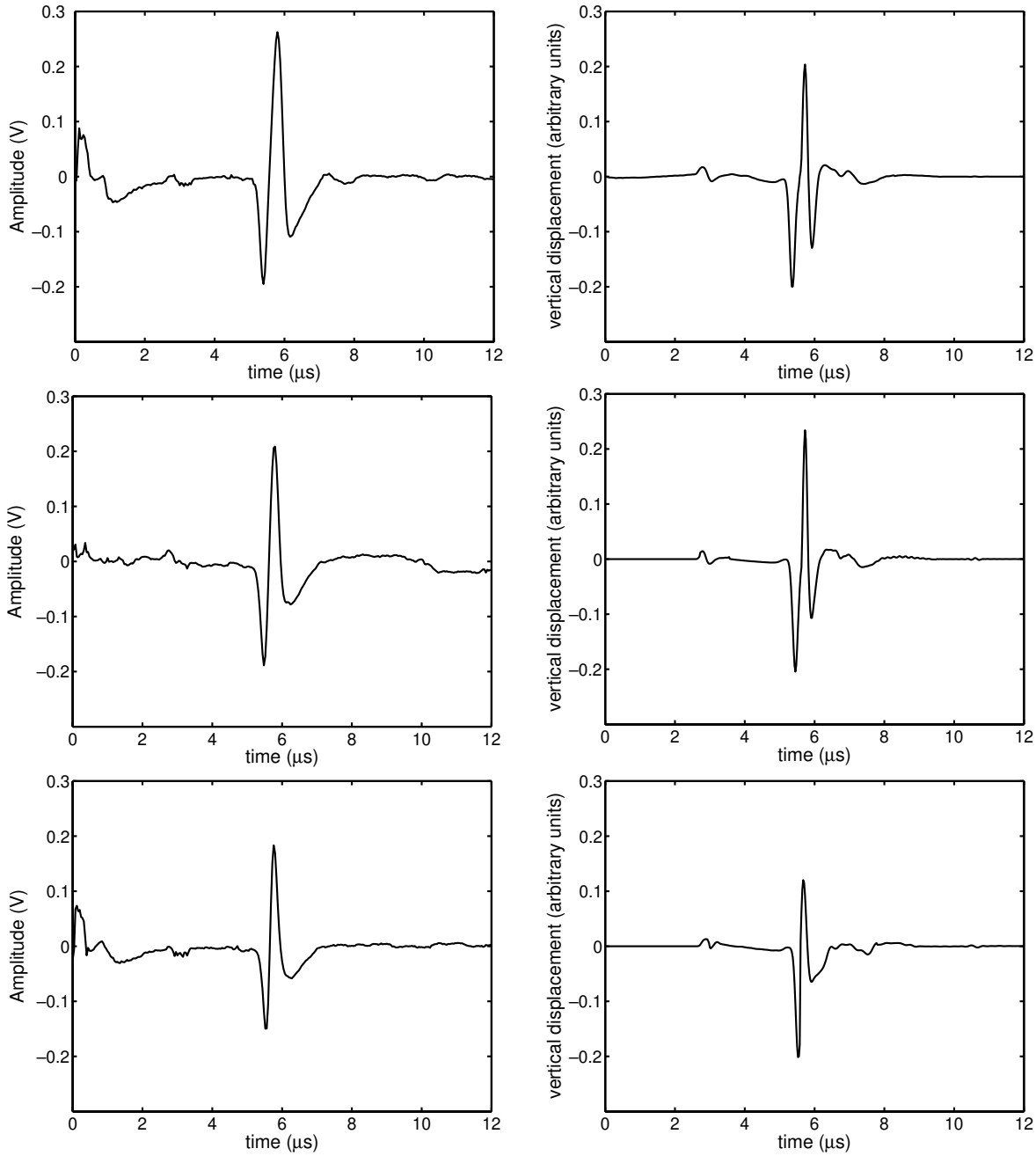

Fig. 9. Experimental (left column) and simulated (right column) signals at the receiver when the laser is located at distances of 0.75, 0.5 and 0.25 mm from the left face of the notch.

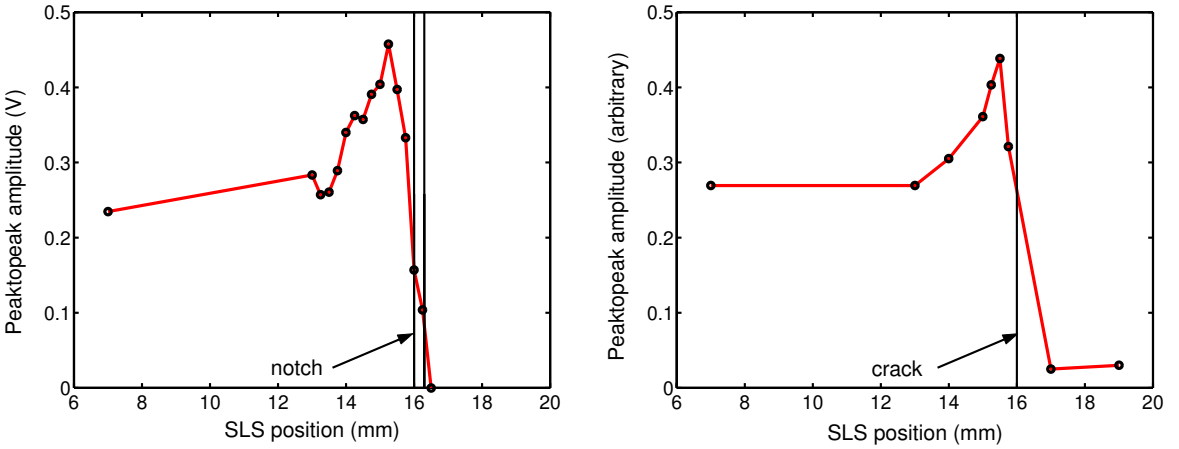

Fig. 10. Experimental (left) and simulated (right) peak-to-peak amplitude vs. position of the source relative to the crack (SLS position).

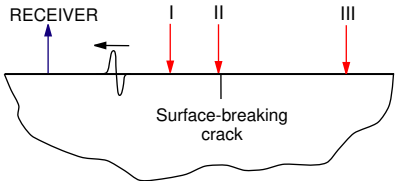

Fig. 11. Configuration for the SLS technique. Three positions of the laser line-source (I–III) are displayed.

When the laser source is far away from the crack, the direct signal can be clearly differentiated from the reflection. The direct signal is a monopolar inward displacement, as should be expected since the crack at sufficient distance from the illuminated region not to affect the generation process. Thus, the shape of the direct signal agrees with those shown in Fig. 3 for laser generation in a defect-free half-space. The reflected signal is also a monopolar

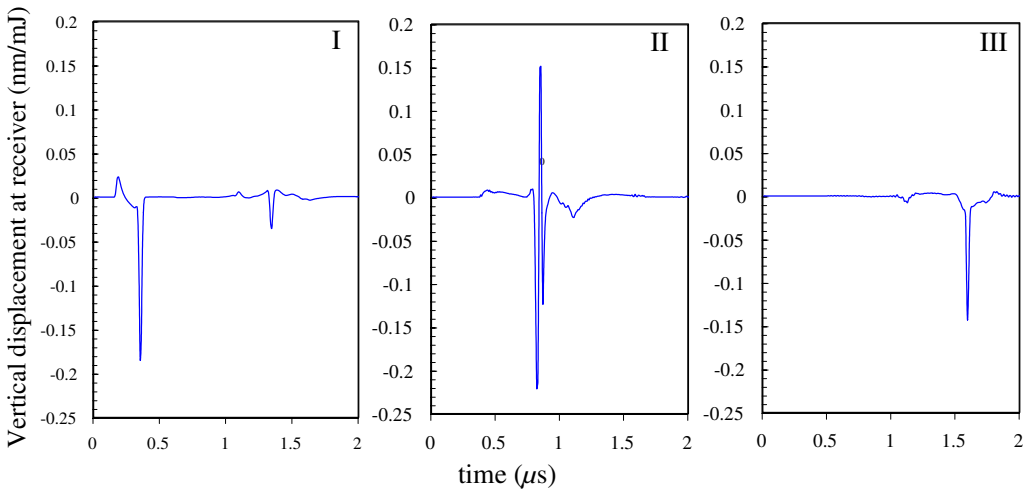

Fig. 12. Characteristic time signal at receiver simulated for three different positions of the laser source relative to the crack.

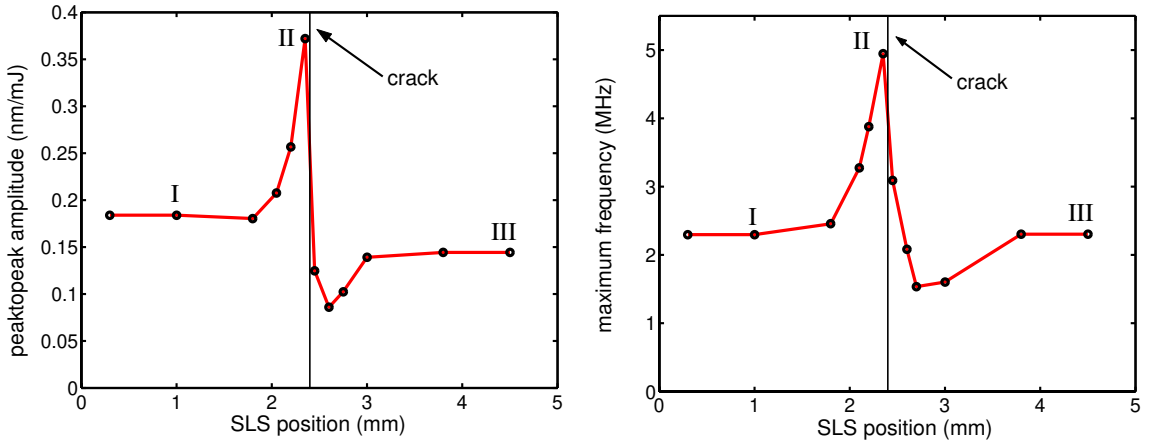

Fig. 13. Simulated signatures of the defect in the ultrasonic amplitude (left) and the maximum frequency (right) of the generated signal as the laser source scans over a surface-breaking crack.

inward displacement. As the laser source approaches the crack, the signal at the receiver becomes clearly bipolar and its amplitude increases significantly. This phenomenon could be related to scattering of body waves and mode conversion at the corner edge of the crack, as well as changes in the generation conditions.

The peak-to-peak amplitude and the maximum frequency of the Rayleigh wave have been plotted versus the SLS position (see Fig. 13). The proposed model reproduces the characteristic variations observed experimentally as the SLS passes over the defect [1].

It should be noted that the difference between the amplitude level far ahead and far behind the crack is related to the depth of the crack relative to the center wavelength of the generated Rayleigh surface wave. Here, the depth of the crack is approximately 1/3 of the center wavelength, so that a substantial portion of the incident energy is transmitted past the crack. Such a small crack produces weak echoes, and would be difficult to detect by a conventional technique. By contrast, Fig. 13 shows that the increase in the peak-to-peak amplitude as the laser source approaches the position of the crack is significant even for such a small crack. These results illustrate the enhanced sensitivity of the SLS technique as compared to conventional methods. It also illustrates the potential capabilities of this technique in the sizing of the defect.

5. Conclusions

A model for the scanning laser source (SLS) technique for the ultrasonic detection of surface-breaking cracks has been presented. The generation of ultrasound by a line-focused laser source on a two-dimensional homogeneous, isotropic, linearly elastic half-space in the presence of a surface-breaking crack has been analyzed. The modeling approach is based on a decomposition of the generated field in the presence of the defect into the incident and the scattered fields. The incident field is that generated by the laser on a defect-free half-space. A thermoelastic model has been used which takes account of the effects of thermal diffusion from the source, as well as the finite width and duration of the laser source. The scattered field incorporates the interactions of the incident field with the discontinuity. It has been analyzed numerically by the boundary element method. A special treatment of the infinite boundary has been used which eliminates spurious reflections from the ends of the computational boundary. The SLS simulations are obtained by superposition of these two fields.

It is shown that the experimentally observed features characterizing the presence and size of surface-breaking cracks are well reproduced by the model. A comparison of experimental and simulated signals at the receiver for the

case of a large notch shows good qualitative agreement. Further adjustment of the parameters of the model is needed for a better quantitative agreement. An illustrative example with a very small surface-breaking crack demonstrates the ability of this inspection method to detect cracks smaller than the wavelength of the generated Rayleigh wave.

Acknowledgements

This paper is based upon work partially supported by the Federal Aviation Administration under Contract #DFTA03-98-F-IA029, and partially supported by the Office of Naval Research under Contract N00014-89-J-1362. The discussions and experimental results provided by Younghoon Sohn and Prof. Krishnaswamy are gratefully acknowledged, as well as the computing resources generously provided by Profs. Wing Kam Liu and Ted Belytschko.

References

[1] A.K. Kromine, P.A. Fomitchov, S. Krishnaswamy, J.D. Achenbach, Laser ultrasonic detection of surface-breaking discontinuities: scanning laser source technique, Mater. Eval. 58 (2000) 173–177.
[2] A.K. Kromine, P.A. Fomitchov, S. Krishnaswamy, J.D. Achenbach, Scanning laser source technique for detection of surface-breaking and sub-surface cracks, in: D. Thompson, D. Chimenti (Eds.), Review of Progress in Quantitative Nondestructive Evaluation, vol. 19, AIP Press, New York, 2000, pp. 335–342.
[3] A.K. Kromine, P.A. Fomitchov, S. Krishnaswamy, J.D. Achenbach, Detection of subsurface defects using laser based technique, in: D. Thompson, D. Chimenti (Eds.), Review of Progress in Quantitative Nondestructive Evaluation, vol. 20, AIP Press, New York, 2001, pp. 1612–1617.
[4] P.A. Fomitchov, A.K. Kromine, Y. Sohn, S. Krishnaswamy, J.D. Achenbach, Ultrasonic imaging of small surface-breaking defects using scanning laser source technique, in: D. Thompson, D. Chimenti (Eds.), Review of Progress in Quantitative Nondestructive Evaluation, vol. 21, AIP Press, New York, 2002, pp. 356–362.
[5] Y. Sohn, S. Krishnaswamy, Mass spring lattice modeling of the scanning laser source technique, Ultrasonics 39 (2002) 543–552.
[6] D.A. Hutchins, Ultrasonic generation by pulsed lasers, in: W.P. Mason, R.N. Thurston (Eds.), Physical Acoustics, vol. XVIII, Academic, San Diego, 1988, Chapter 2, pp. 21–123.
[7] C.B. Scruby, L.E. Drain, Laser Ultrasonics: Techniques and Applications, Adam Hilger, New York, 1990.
[8] P.A. Doyle, On epicentral waveforms for laser-generated ultrasound, J. Phys. D 19 (1986) 1613–1623.
[9] I. Arias, J.D. Achenbach, Thermoelastic generation of ultrasound by line-focused laser irradiation, Int. J. Solids Struct. 40 (2004) 6917–6935.
[10] U. Schleichert, K.J. Langenberg, W. Arnold, S. Fassbender, A quantitative theory of laser-generated ultrasound, in: D. Thompson, D. Chimenti (Eds.), Review of Progress in Quantitative Nondestructive Evaluation, vol. 8A, AIP Press, New York, 1989, pp. 489–496.
[11] W.H. Press, B.P. Flannery, S.A. Teulosky, W.T. Vetterling, Numerical Recipes: The Art of Scientific Computing, 3rd ed., Cambridge University Press, Cambridge, 1986.
[12] K.S. Crump, Numerical inversion of Laplace transforms using a Fourier series approximation, J. ACM 23 (1976) 89–96.
[13] Y. Niwa, S. Hirose, M. Kitahara, Application of the boundary integral equation (BIE) method to transient response analysis of inclusions in a half-space, Wave Motion 8 (1986) 77–91.
[14] J. Domínguez, Boundary Elements in Dynamics, Computational Mechanics Publications, Elsevier Applied Science, Amsterdam, 1993.
[15] G.E. Blandford, A.R. Ingraffea, J.A. Liggett, Two-dimensional stress intensity factor computations using the boundary element method, Int. J. Numer. Meth. Eng. 17 (1981) 387–404.
[16] T.A. Cruse, Fracture mechanics, in: D.E. Beskos (Ed.), Boundary Element Methods in Mechanics, North-Holland, Amsterdam, 1987, pp. 333–365.
[17] I. Arias, J.D. Achenbach, Rayleigh wave correction for the BEM analysis of two-dimensional elastodynamic problems in a half-space, Int. J. Nuner. Meth. Eng., in press.
[18] Y. Sohn, S. Krishnaswamy, Private communication.